Pergamon

Int. J. Heat Mass Transfer. Vol. 40, No. 6, pp. 1343–1354, 1997

0017–9310/97 $17.00+0.00

PII: S0017–9310(96)00210–4

A numerical analysis of solid–liquid phase change heat transfer around a single and two horizontal, vertically spaced cylinders in a rectangular cavity

K. SASAGUCHI
Department of Mechanical Engineering, Kumamoto University, Kumamoto 860, Japan

K. KUSANO
Graduate School of Science and Technology, Kumamoto University, Kumamoto 860, Japan

and

R. VISKANTA
School of Mechanical Engineering, Purdue University, West Lafayette, IN 47907, U.S.A.

(*Received* 18 *December* 1995 *and in final form* 28 *May* 1996)

Abstract—In the present study, a new numerical model is proposed to analyze solid–liquid phase change heat transfer in a complicated geometry. The present model can treat the solid/liquid phase change heat transfer with/without porous media, as well as conventional transient natural convection with/without porous media. Solidification calculations of pure water (without porous media) around a single cylinder and two cylinders were performed to check the validity of the model. The interaction of two solidification layers were examined, and the effects of natural convection in the melt on the solidification process were also studied. The numerical results were found to be in excellent agreement with experimental data. It was also shown that for the initial water-temperature, T_i, of 0°C the solidification progresses more rapidly for the single cylinder than that for the two cylinders, but the reverse is true for $T_i \geqslant 4$°C. Copyright © 1996 Elsevier Science Ltd.

1. INTRODUCTION

Solid–liquid phase change heat transfer around cylinder(s) occurs in many systems and in nature including latent heat thermal energy storage, freezing/thawing of soil, and others. Recently, for the purpose of effective load levelling of electric power at night, much attention has been given to ice thermal energy storage systems. Understanding of the solid–liquid phase change heat transfer phenomena around two or more cylinders is needed for design of efficient latent heat-of-fusion energy storage systems. These important applications have motivated recent studies on the subject. Using fluids without density inversion, solidification studies have been conducted around a single cylinder [1] as well as melting/solidification around two or more cylinders [2–4]. Using water, which is a very important phase change material (PCM) for ice thermal energy storage, solidification around a single cylinder [5, 6] as well as solidification or melting around two or more cylinders [7–9] have been investigated.

Past studies of solid–liquid phase change heat transfer around two or more cylinders were restricted to experimentation because of complicated coordinate systems needed for numerical analysis. Recently, Lacroix [10] proposed a numerical model for analyzing phase change heat transfer around two cylinders in a rectangular cavity and numerically simulated cyclic melting and resolidification of a paraffin wax, which was experimentally studied by Sasaguchi and Viskanta [3]. However, since Lacroix uses a stream function-vorticity formulation, it is difficult to determine the vorticity at the solid–liquid interface with this model. In addition, his model can not treat the solid/liquid phase change heat transfer in porous media, which is a very important application for freezing of water saturated soil.

The authors have proposed a numerical model [11] to simulate the solid–liquid phase change heat transfer in water saturated porous media confined in a rectangular cavity using the primitive variables, i.e. velocities, pressure and temperature. In the present study, the previous model [11] has been extended to a generalized coordinate system, to enable analysis of complicated phase change heat transfer problems around

NOMENCLATURE

A_c	total cross-sectional area of cylinder(s)
A_s	solidified area
a	thermal diffusivity
c	specific heat
d	diameter of the cylinder
g	gravitational acceleration vector
h_f	latent heat of fusion
(i,j)	grid point
K	permeability
P	dimensionless pressure, $d^2p/(\rho a_\ell^2)$
p	pressure
T	temperature
t	time
U, V	x-, y-direction dimensionless velocity–vector component, $d\cdot u/a_\ell$, $d\cdot v/a_\ell$
$\mathbf{u}$	velocity vector
u, v	x-, y-direction velocity-vector components
X, Y	dimensionless coordinate axes, x/d, y/d
x, y	coordinate axes (see Fig. 2).

Greek symbols

γ	volume fraction
ε	porosity
Λ	dimensionless thermal conductivity, λ/λ_ℓ
λ	thermal conductivity
ν	kinematic viscosity
θ	dimensionless temperature, $(T-T_i)/(T_w-T_i)$
θ_{PH}	dimensionless fusion temperature, $(T_{PH}-T_i)/(T_w-T_i)$
ξ, η	transformed coordinate axes (see Fig. 2)
Π	dimensionless density, ρ/ρ_ℓ
Ω	dimensionless specific heat, c/c_ℓ
Ω_s	dimensionless specific heat ratio, c_s/c_ℓ
Λ_s	dimensionless thermal conductivity ratio, λ_s/λ_ℓ
ρ	density
τ	dimensionless time, $a_\ell t/d^2$
τ_s	dimensionless time, $a_s t/d^2$
ϕ	variables, U, V, P, θ, or γ in equations (13) and (14).

Subscripts

i	initial
ℓ	liquid phase
m	melting
p	porous particles
PH	fusion point
ref	reference value
w	cylinder surface
s	solid phase or solidification
x, y	derivatives with respect to x, y
ξ, η	derivatives with respect to ξ, η.

Superscript

n	the number of iterations.

two or more cylinders in a rectangular cavity. The primitive variables were also used in the extended model to eliminate the complicated determination of the vorticity at the solid–liquid interface. The present model can treat solid–liquid phase change heat transfer with/without porous media and can also handle the conventional transient natural convection with/without porous media. With the new model, calculations were performed for freezing of pure water (without porous media) around a single cylinder and two cylinders. The results were compared with experimental data to check the validity of the model, and the effects of the initial temperature of the water and the number of cylinders on the solidification process were systematically examined.

2. PHYSICAL/NUMERICAL MODEL AND GOVERNING EQUATIONS

A proposed model can be adapted for both solidification and melting processes as well as for various tube arrangements and different geometries of the surrounding boundaries. However, the model is explained using a specific physical system for which the numerical analysis was performed in this paper to facilitate easier understanding. Figure 1 shows the physical system. It consists of a rectangular cavity which contains two horizontal, vertically spaced cylinders with diameter d, and all the walls (left, right, top and bottom walls) are assumed to be insulated. In this study d is set at 0.0254 m, and the height and width of the enclosure as well as the position of the cylinders are arbitrarily set without considering a particular device, as shown in Fig. 1. The cavity is filled with water as the PCM. For comparison, calculations for a single cylinder (i.e. the upper cylinder was removed) were also performed. Initially, the PCM is in the solid (liquid) phase at a uniform temperature, T_i. At time $t = 0$ s, the temperature of the cylinders is suddenly changed and maintained at a prescribed value, T_w, which is smaller (larger) than the fusion temperature, and the solidification (melting) process is initiated.

For simplicity, the following assumptions are made in the analysis: (1) the flow is two-dimensional, laminar and incompressible; (2) the liquid density varies only in the buoyancy term, i.e. PCM is the Boussinesq liquid; (3) the solid phase is at rest; (4) the density

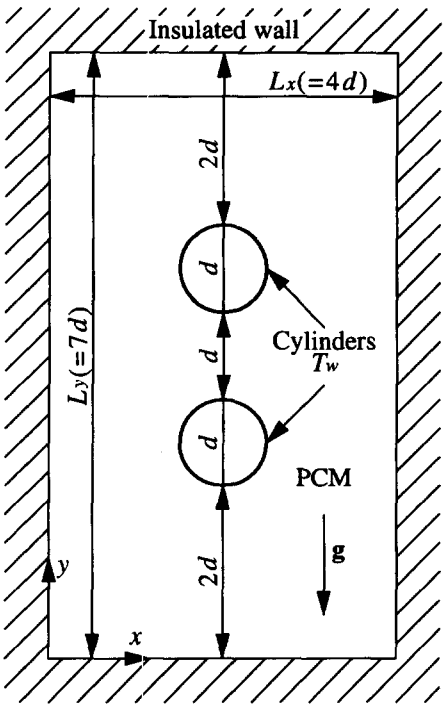

Fig. 1. Physical model.

change due to solid–liquid phase change is negligible. With these assumptions, the dimensional governing equations, which can also treat solid–liquid phase change problems in a liquid saturated porous media, may be derived for a single domain model [11–13] as follows:

continuity

$$\nabla \cdot \mathbf{u} = 0 \tag{1}$$

momentum

$$\rho \frac{\partial \mathbf{u}}{\partial t} + \rho(\mathbf{u}\cdot\nabla)\mathbf{u} = -\nabla p + \rho \nu_\ell \Delta \mathbf{u} - \rho \frac{\nu_\ell}{K(\gamma_\ell)}\mathbf{u} + (\rho_{\text{ref}} - \rho)\boldsymbol{g} \tag{2}$$

energy equation

$$\rho c \frac{\partial T}{\partial t} + \rho c_\ell (\mathbf{u}\cdot\nabla)T = \nabla\cdot(\lambda \nabla T) - \rho_\ell h_{\text{f}} \frac{\partial \gamma_\ell}{\partial t}. \tag{3}$$

These conservation equations were obtained by summing conservation equations for all phases in a control volume. The density, specific heat and thermal conductivity in the equations (1)–(3) for a porous medium are defined as follows:

$$\rho = (1-\varepsilon)\rho_{\text{p}} + (\varepsilon - \gamma_\ell)\rho_{\text{s}} + \gamma_\ell \rho_\ell \tag{4}$$

$$\rho c = (1-\varepsilon)\rho_{\text{p}} c_{\text{p}} + (\varepsilon - \gamma_\ell)\rho_{\text{s}} c_{\text{s}} + \gamma_\ell \rho_\ell c_\ell \tag{5}$$

$$\lambda = (1-\varepsilon)\lambda_{\text{p}} + (\varepsilon - \gamma_\ell)\lambda_{\text{s}} + \gamma_\ell \lambda_\ell. \tag{6}$$

The porosity ε is defined as the ratio of the volume occupied by the solid and liquid phases of the fluid to the total control volume considered, and it is taken to be a constant. The volumetric liquid fraction, γ_ℓ, is the ratio of the volume occupied by the liquid phase of the fluid to the total volume, it varies during phase transformation. The expression, equation (6), for the averaged thermal conductivity derived in the present model is the same as that based on the so-called 'parallel model' which gives an upper limit. If we consider a system which contains a PCM and a porous medium whose thermal conductivities are not largely different, equation (6) gives a reasonable value, but if the difference is very large, some modification seems to be needed. For a system without porous media, as considered in the calculations described later, if the thermal conductivities of the solid and liquid phases of PCM are not largely different, which is true for a large number of PCM, the expression gives good approximation for the averaged thermal conductivity.

The single set of governing equations (1)–(3) is solved in the entire region, meaning that no special consideration is needed on the interface. The third term on the right-hand side of equation (2) is the Darcy term expressing the resistance to the fluid flow, which is caused by the porous media and the solid phase in the solid–liquid coexistent control-volumes. The permeability, K, is a function of γ_ℓ. Inclusion of the Darcy term automatically ensures that the velocity in perfectly-solidified control volumes vanishes, since the permeability becomes zero in the volumes. Therefore, the Darcy term itself becomes infinite, resulting in zero velocity. In the buoyancy term (i.e. the fourth term on the right-hand side of equation (2)), the following density–temperature relationship of water proposed in ref. [14] was adopted for the liquid density, ρ_ℓ:

$$\rho_\ell = \rho_{\ell\max}(1 - \omega|T - T_{\max}|^q) \tag{7}$$

where $\rho_{\ell\max} = 999.972$ kg m^{-3}, $\omega = 9.297173 \times 10^{-6}$°C^{-q}, $T_{\max} = 4.0293$°C and $q = 1.894816$. This relationship takes into account the nature of the density-inversion in water, and it is introduced into the fourth term in equation (2) with equation (4). The second term on the right-hand side of equation (3) is a source term related to phase change. With this term in the energy equation (3), we do not need special treatment to track the interface motion. The value of γ_ℓ in the control volumes undergoing phase change can be evaluated using the following iterative expression [15]:

$$\gamma_\ell^{n+1} = \gamma_\ell^n + \frac{(\rho c)^n}{\rho_\ell h_{\text{f}}}(T^n - T_{\text{PH}}). \tag{8}$$

The limitation imposed on the equation is that the condition

$$0 \leqslant \gamma_\ell \leqslant \varepsilon \tag{9}$$

is satisfied.

Introduction of the Cartesian coordinate system (x-y-system) into a complicated physical domain requires

interpolation of the variables, i.e. velocities, temperature and pressure, on some boundaries since the grids are not necessarily coincident with them. To eliminate the errors and complexity due to this interpretation, the governing equations are transformed into a generalized coordinate system, and calculations are performed on the transformed plane. For example, the energy equation (in dimensionless form) in the Cartesian coordinate system,

$$\frac{\partial\theta}{\partial\tau}+\frac{1}{\Omega}(\mathbf{U}\cdot\nabla)\theta=\frac{1}{\Pi\Omega}\nabla\cdot(\Lambda\nabla\theta)+S_{\mathrm{h}} \tag{10}$$

is transformed into the following equation in the generalized coordinate system,

$$\begin{aligned}\frac{\partial\theta}{\partial T}&+\frac{1}{\Omega J}\{(Y_\eta U-X_\eta V)\theta_\xi+(X_\xi V-Y_\xi U)\theta_\eta\}\\&=\frac{1}{\Pi\Omega J^2}\{(Y_\eta\Lambda_\xi-Y_\xi\Lambda_\eta)(Y_\eta\theta_\xi-Y_\xi\theta_\eta)\\&\quad+(X_\eta\Lambda_\xi-X_\xi\Lambda_\eta)(X_\eta\theta_\xi-X_\xi\theta_\eta)\}\\&\quad+\frac{1}{\Pi\Omega J^2}\{(X_\eta^2+Y_\eta^2)\theta_{\xi\xi}-2(X_\xi X_\eta+Y_\xi Y_\eta)\theta_{\xi\eta}\\&\quad+(X_\xi^2+Y_\xi^2)\theta_{\eta\eta}\}+\frac{1}{\Pi\Omega J}\{A(Y_\xi\theta_\eta-Y_\eta\theta_\xi)\\&\quad+B(X_\eta\theta_\xi-X_\xi\theta_\eta)\}+S_{\mathrm{h}}.\end{aligned} \tag{11}$$

The source term, S_{h}, in the above equation is defined as follows:

$$S_{\mathrm{h}}=\begin{cases}-\dfrac{\Omega_{\mathrm{s}}}{\Pi\Omega}\cdot\dfrac{\theta_{\mathrm{PH}}-1}{\mathrm{Ste}_{\mathrm{s}}}\cdot\dfrac{\partial\gamma_\ell}{\partial\tau} & \text{for solidification}\\[2ex] -\dfrac{1}{\Omega\Pi}\cdot\dfrac{1-\theta_{\mathrm{PH}}}{\mathrm{Ste}_{\mathrm{m}}}\cdot\dfrac{\partial\gamma_\ell}{\partial\tau} & \text{for melting}\end{cases} \tag{12}$$

where

$$Ste_{\mathrm{s}}=\frac{c_{\mathrm{s}}(T_{\mathrm{PH}}-T_{\mathrm{w}})}{h_{\mathrm{f}}},\quad\text{and}\quad Ste_{\mathrm{m}}=\frac{c_\ell(T_{\mathrm{w}}-T_{\mathrm{PH}})}{h_{\mathrm{f}}}.$$

In equations (10–12),

$$X=\frac{x}{d}\quad Y=\frac{y}{d}\quad\tau=\frac{a_\ell}{d^2}t$$

$$U=\frac{d}{a_\ell}u\quad V=\frac{d}{a_\ell}v\quad\theta=\frac{T-T_{\mathrm{i}}}{T_{\mathrm{w}}-T_{\mathrm{i}}}$$

$$\Pi=\frac{\rho}{\rho_\ell}=(1-\gamma_\ell)\frac{\rho_{\mathrm{s}}}{\rho_\ell}+\gamma_\ell=1\quad(\text{assuming}\quad\rho_{\mathrm{s}}=\rho_\ell)$$

$$\Omega=\frac{c}{c_\ell}=\frac{1}{\Pi}[(1-\gamma_\ell)\Omega_{\mathrm{s}}+\gamma_\ell]$$

$$\Lambda=\frac{\lambda}{\lambda_\ell}=(1-\gamma_\ell)\Lambda_{\mathrm{s}}+\gamma_\ell$$

$$\Omega_{\mathrm{s}}=\frac{c_{\mathrm{s}}}{c_\ell}\quad\Lambda_{\mathrm{s}}=\frac{\lambda_{\mathrm{s}}}{\lambda_\ell}$$

$$J=X_\xi Y_\eta-X_\eta Y_\xi$$

$$\begin{aligned}A&=(X_\eta^2+Y_\eta^2)X_{\xi\xi}-2(X_\xi X_\eta\\&\quad+Y_\xi Y_\eta)X_{\xi\eta}+(X_\xi^2+Y_\xi^2)X_{\eta\eta}\end{aligned}$$

$$\begin{aligned}B&=(X_\eta^2+Y_\eta^2)Y_{\xi\xi}-2(X_\xi X_\eta+Y_\xi Y_\eta)Y_{\xi\eta}\\&\quad+(X_\xi^2+Y_\xi^2)Y_{\eta\eta}.\end{aligned}$$

A complete set of the dimensionless governing equations and the transformed equations to the generalized coordinate system can be seen in reference [16].

In addition to transforming the governing conservation equations into the generalized coordinate system, it is necessary to adapt the grid lines in the generalized coordinate system to the physical boundaries of the system by properly generating the grids in the physical domain. In the present study, we adopted a numerical, grid generation technique proposed by Steger and Sorenson [17]. The following equations are used to generate the computational grids:

$$\begin{aligned}(X_\eta^2+Y_\eta^2)X_{\xi\xi}&-2(X_\xi X_\eta+Y_\xi Y_\eta)X_{\xi\eta}+(X_\xi^2+Y_\xi^2)X_{\eta\eta}\\&+J^2(PX_\xi+QX_\eta)=0\\(X_\eta^2+Y_\eta^2)Y_{\xi\xi}&-2(X_\xi X_\eta+Y_\xi Y_\eta)Y_{\xi\eta}+(X_\xi^2+Y_\xi^2)Y_{\eta\eta}\\&+J^2(PY_\xi+QY_\eta)=0\end{aligned} \tag{13}$$

where P and Q in equation (13) are functions related to the grid density control. The transformation of the governing equations into the generalized coordinate system makes the governing equations in the computational plane more complicated. However, the calculations can be performed in a simple computational-plane, e.g. a rectangular domain, with a uniformly-spaced grid system. In addition, since the boundaries in the computational plane are coincident with the physical boundaries, the interpolations on the boundaries are not needed. Therefore, accurate results can be obtained.

Figure 2(a) and (b) shows the grid systems generated by using the technique described above for the single cylinder and the two-cylinder arrangement, respectively. Experimental results (flow patterns and solid–liquid interface shapes) showed that fluid flow and heat transfer were symmetrical about the vertical center line of the cavity. Therefore, we need to consider only half of the domain. The right panel of each figure represents the grid system in the computational plane. The left of it shows the transformed grid from the computational plane into the physical plane. Points indicated by the numbers in the physical and computational planes correspond each other. In this study, we chose a $31(\xi)\times101(\eta)$ uniform mesh in the computational plane for the single-cylinder-case and a 31×121 mesh for the two-cylinder-case. With these mesh systems, we can obtain satisfactory agreement between the numerical predictions and experimental data as will be shown in Section 3.1. The governing

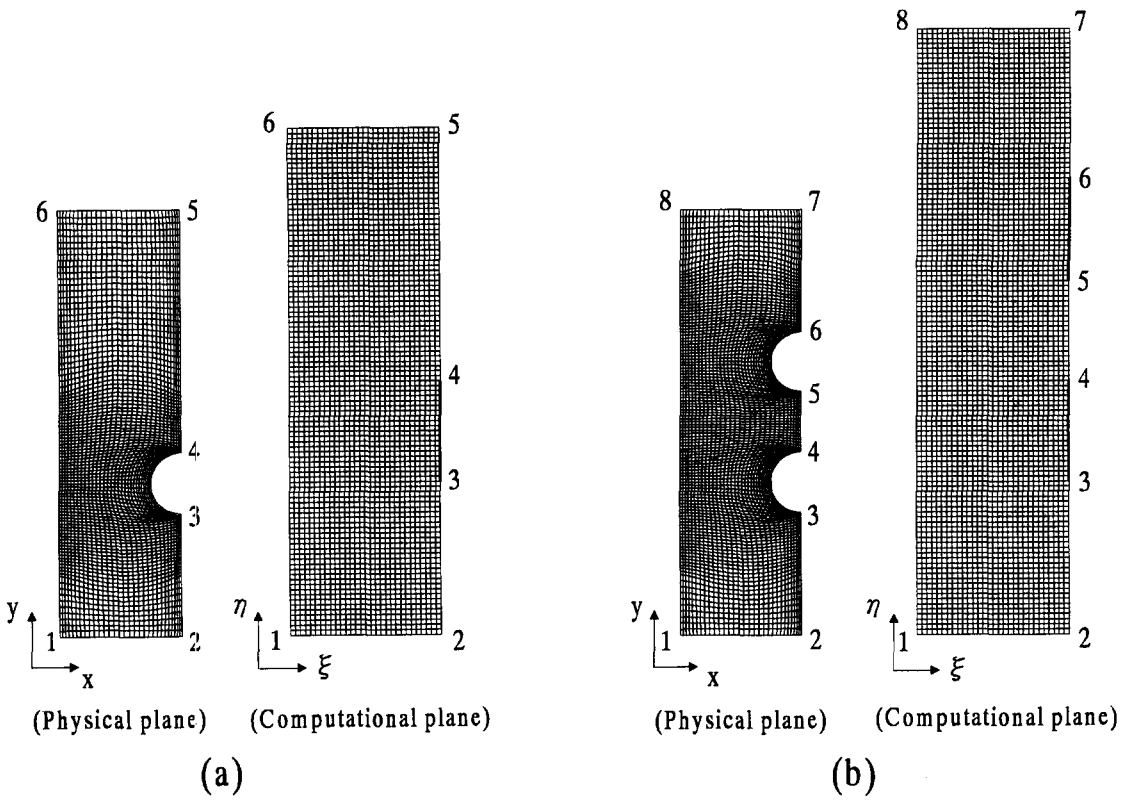

Fig. 2. Grid systems: (a) single-cylinder; (b) two-cylinder arrangement.

equations in the generalized coordinate system, such as equation (11), were discretized based on the MAC algorithm [18], and they were solved iteratively. Detailed numerical procedure is given in ref. [16]. The calculations are repeated at the same time-step until the following criteria are satisfied:

- for the dimensionless velocities U and V, and the dimensionless pressure, P,

$$\frac{\max|\phi^{n+1}(i,j)-\phi^{n}(i,j)|}{\max|\phi^{n+1}(i,j)|}<10^{-4} \tag{14}$$

- for the dimensionless temperature, θ, and the volumetric liquid fraction, γ_ℓ

$$\max\left(\frac{|\phi^{n+1}(i,j)-\phi^{n}(i,j)|}{|\phi^{n+1}(i,j)|}\right)<10^{-4}. \tag{15}$$

3. RESULTS AND DISCUSSION

3.1. *Comparison between numerical predictions and experimental data*

Since solidification of pure water without porous media is considered in the present study, the porosity, ε, is set to unity, and the permeability, $K(\gamma_\ell)$, in the third term on the right-hand side of equation (2), was assumed to be given by

$$\frac{1}{K(\gamma_\ell)}=\frac{(1-\gamma_\ell)}{d^2}\times 10^{30}. \tag{16}$$

In the above equation, we adopt a similar relation used in the literature [13, 19].

To check the validity of the present model, we first performed several validations by comparing model predictions with experimental data. The diameter of the cylinders was 0.0254 m, and we used the measured value as the cylinder temperatures, T_w, in the calculations in order to use the same temperature boundary-conditions between the numerical calculations and the measurements. In the experiments, the cylinder temperatures reached a prescribed value of $-10°C$ at $t\approx 60$ s (see ref. [9] for details of the experiments).

Figure 3 shows timewise variations of solid–liquid interface shapes for an initial water temperature of $T_i=4°C$. Figure 3(a) and (b) shows the development of the solid/liquid front around a single and two cylinder(s), respectively. Figure 4 illustrates the timewise variations of the solid volume ratio, A_s/A_c, which is defined as the ratio of the solidified area to the total cross-sectional area of the cylinder(s). Note that for the two-cylinder arrangement, the total area of the cylinders is twice as large as that of the single-cylinder. The predicted interface shapes and the solid volume ratios are in excellent agreement with the experimental data in the entire time range. The predicted flow patterns (not shown) also agree well with experimental results. From these findings, we conclude that the present numerical model is valid even for the freezing of water on the complicated geometry.

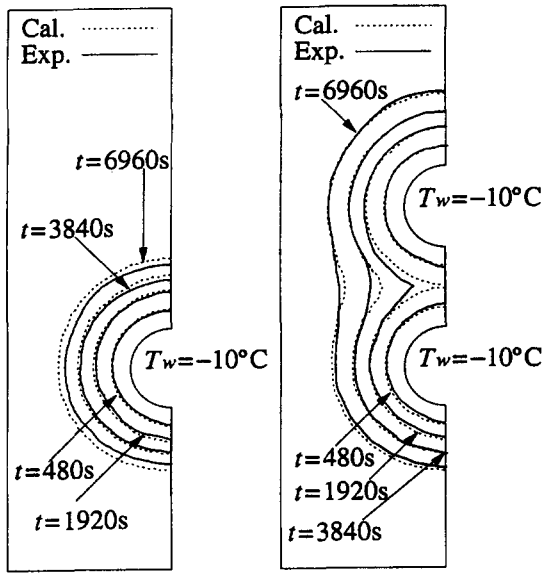

Fig. 3. Timewise variations of solid–liquid interface for $T_i = 4°C$ and $T_w = -10°C$: (a) single-cylinder; (b) two-cylinder arrangement.

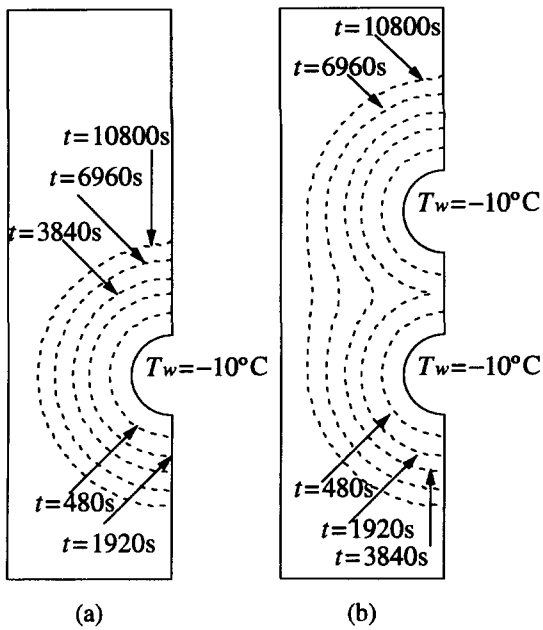

Fig. 5. Timewise variations of the solid-liquid interface positions for $T_i = 0°C$ and $T_w = -10°C$: (a) single-cylinder; (b) two-cylinder arrangement.

3.2. *Results for* $T_i = 0°C$

In order to examine in detail the effect of the initial temperature of water in the solidification, calculations were performed for $T_i = 0, 4, 8$ and $12°C$. The cylinder temperature was set at $-10°C$ for $t \geqslant 0$ s.

Figures 5 and 6 show the timewise variations of the interface shape and the solid volume ratio for $T_i = 0°C$, respectively. In Fig. 6, a dimensionless time τ_s is used as an abscissa in addition to the physical time t. In this case, no flows arise in water, and conduction is the sole mode of the heat transfer. Hence, only the energy equation was solved in which the convective terms were absent. For the solidification around a single cylinder (Fig. 5(a)), the solid layers develop concentrically around the cylinder. In the case of the two-cylinder arrangement (Fig. 5(b)), the solid layers develop concentrically around the upper and lower cylinders at early times (e.g. see the solid layers at $t = 480$ s). At later times ($t \approx 1920$ s), the solid layers around the two cylinders interact with each other, but they are still symmetric about the horizontal midline between the cylinders. It is seen from Fig. 6 that the solid volume ratio, A_s/A_c, for the two-cylinder arrangement is coincident with that for the single-cylinder at early stages, but the former becomes gradually smaller than the latter as time progresses ($t > 1920$ s). This is because the surface area of the interface for the two-cylinder arrangement becomes smaller than that for the single-cylinder due to the interaction of the solidification layers developed around the cylinders.

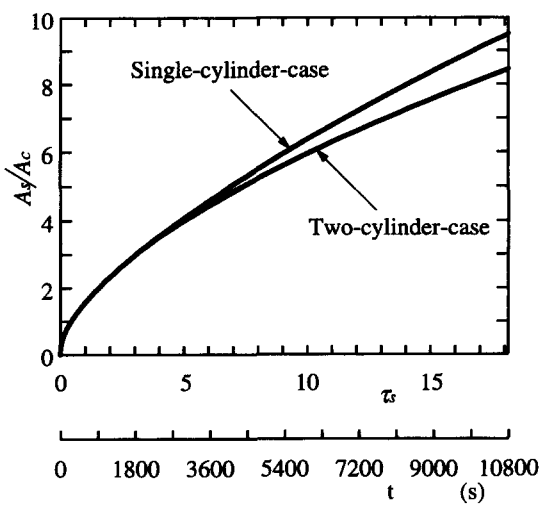

Fig. 6. Comparison of timewise variations of solid volume ratios for $T_i = 0°C$ and $T_w = -10°C$.

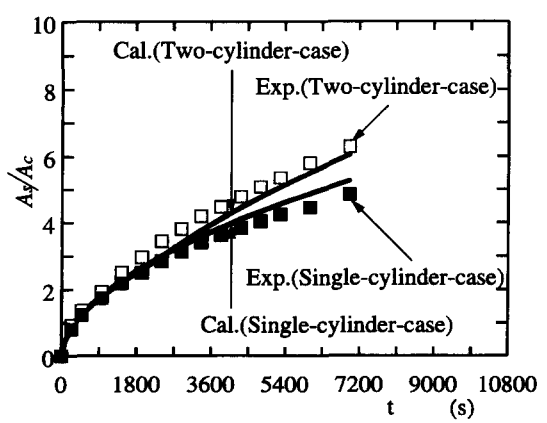

Fig. 4. Comparison of timewise variations of predicted and measured solid volume ratios for $T_i = 4°C$ and $T_w = -10°C$.

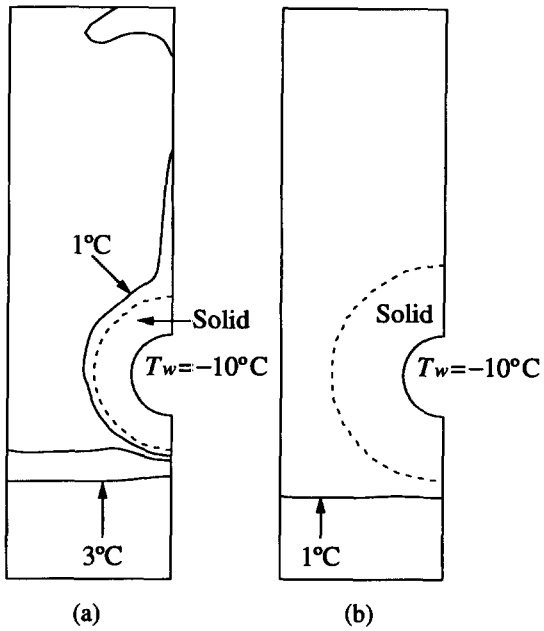

Fig. 7. Timewise variations of temperature field and solid–liquid interface position for the single-cylinder with $T_i = 4°C$ and $T_w = -10°C$: (a) $t = 1920$ s; (b) $t = 6960$ s.

3.3. *Results for* $T_i = 4°C$

The numerical results for $T_i = 4°C$ are shown in Figs. 7–10. The density of water increases with temperature in the range between 0°C and 4°C (the density-inversion); therefore, for $T_i = 4°C$ upward flow arises along the solid–liquid interface at which the temperature is 0°C. As is seen from Fig. 9(a) and (b) at $t = 1920$ s, the upward flow is rather strong, and the cooled water along the interface accumulates in the upper part of the cavity. Consequently, a thermally stratified region is gradually established (Figs. 7(a) and 8(a)). As time progresses, the water temperature in the upper part of the cavity decreases to near the solidification temperature (0°C) and consequently the upward flows are suppressed. At $t = 6960$ s (Figs. 7(b) and 8(b)), the water temperature is almost uniform in the entire cavity, except in the bottom part of the cavity, and almost no flows are evident at this time (not shown). It is seen from Figs. 7(b) and 8(b) that the solidification is slightly faster about the upper part of the cylinder for the single-cylinder and about the

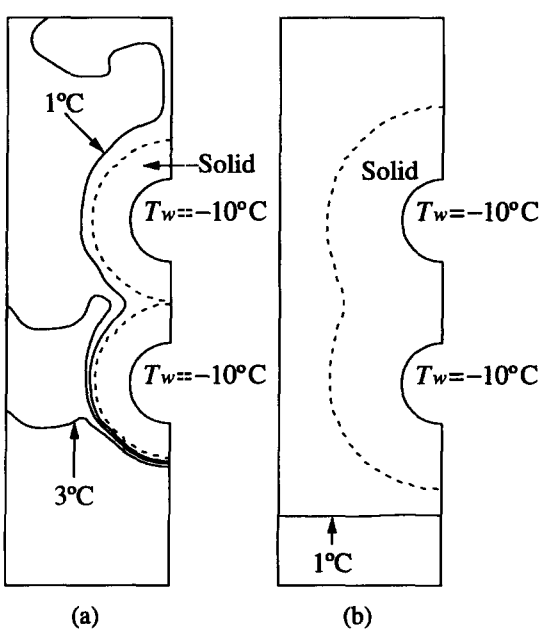

Fig. 8. Timewise variations of temperature field and solid–liquid interface position for the two-cylinder arrangement with $T_i = 4°C$ and $T_w = -10°C$: (a) $t = 1920$ s; (b) $t = 6960$ s.

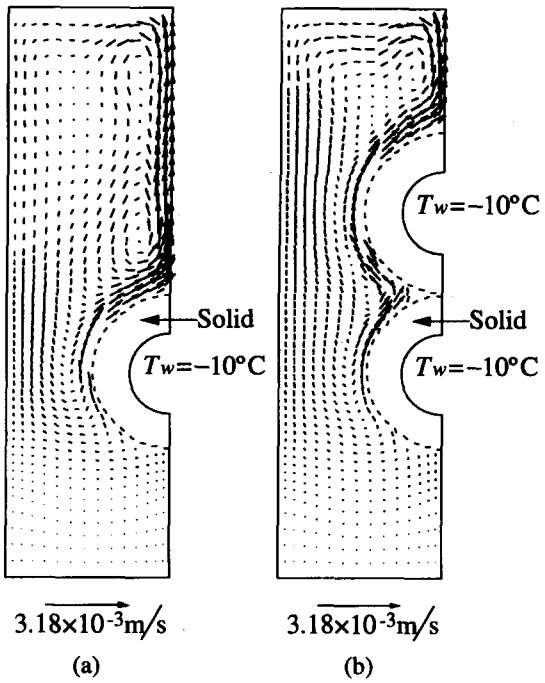

Fig. 9. Velocity field and solid–liquid interface at $t = 1920$ s for $T_i = 4°C$ and $T_w = -10°C$: (a) single-cylinder; (b) two-cylinder arrangement.

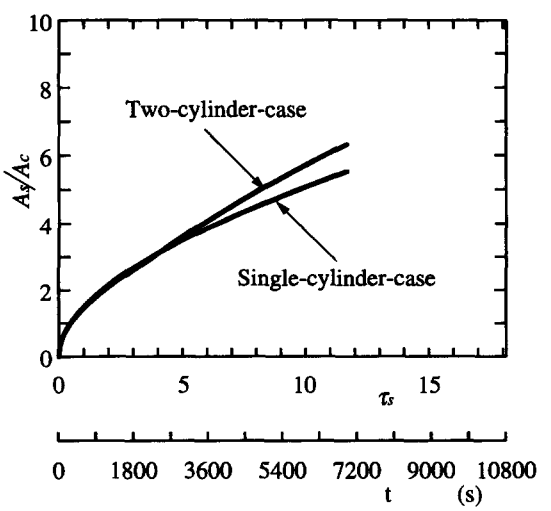

Fig. 10. Comparison of timewise variation of solid volume ratios for $T_i = 4°C$ and $T_w = -10°C$.

upper cylinder for the two-cylinder arrangement, due to the thermal stratification.

In the case of $T_i = 4°C$, the solid volume ratio for the two-cylinder arrangement is larger than that for the single-cylinder after $t \geqslant 3000$ s (Fig. 10). It should be noted that the reverse trend was true for $T_i = 0°C$ (Fig. 6). This is because for $T_i = 4°C$ cooling of water in the upper part of the cavity is much faster for the two-cylinder system due to the strong upward flow than that for the single-cylinder. This prevents the solidification rate (increasing rate of A_s/A_c with respect to time) for the two-cylinder arrangement from decreasing, even after the solid layers interact.

3.4. *Results for* $T_i = 8°C$

When the initial water temperature is 8°C, the temperature and velocity fields become much more complicated since the maximum water density (at $\approx 4°C$) is located at the mid-point between the fusion temperature and T_i. Figures 11 and 12 show the results for the single-cylinder and the two-cylinder arrangement, respectively. At an early times of the solidification process for the single-cylinder (Fig. 11(a)), only a downward flow near the solid/liquid interface is evident since the region where $T > 4°C$ is much larger than that where $T < 4°C$ (the density-inversion region). The water temperature is reduced as the flow descends along the solid–liquid interface, and thus the ice thickness is greater on the lower than on the upper part of the cylinder.

It is seen from Fig. 11(b) at $t = 1920$ s that the cooled water descending along the interface has accumulated around the cylinder, and the region in which the water temperature is below 4°C has been spread. Hence, the density of water near the interface becomes smaller than that on the remote regions away from it. This density field results in a relatively strong upward flow along the interface. However, this flow cannot penetrate into the upper part of the cavity, because the water is thermally stable there. The upward flow becomes weaker with time, but the temperature in the upper part of the cavity is gradually decreased to near the fusion temperature, so that the solidification becomes faster about the upper part of the cylinder. In the bottom part of the cavity, the water temperature is near 4°C and the fluid is stratified. The flow is very weak and the solidification rate is slow.

For the two-cylinder arrangement (Fig. 12), a stronger descending flow is evident along the interface at an early stage than that for the single-cylinder (compare Fig. 12(a) with Fig. 11(a)). Thus, water in the bottom part of the cavity is cooled faster for the two-cylinder arrangement. The accumulation of the cold water changes the direction of the main circulation (Fig. 12(b)), as is also seen for the single-cylinder (Fig. 11(b)). However, the flow is relatively complicated for the two-cylinder arrangement. That is, in addition to an upward flow along a large part of the interface two convection cells appear in the upper region of the cavity. As time progresses, the water is cooled gradu-

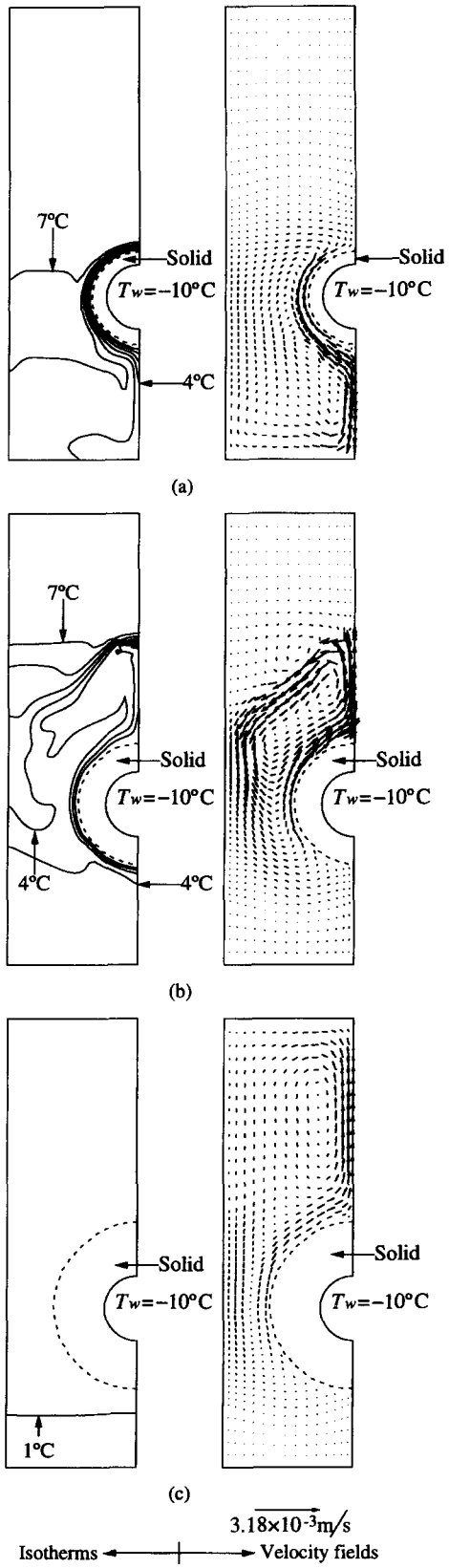

Fig. 11. Temperature (left panels) and velocity (right panels) fields and solid–liquid interface positions for the single-cylinder with $T_i = 8°C$ and $T_w = -10°C$: (a) $t = 480$ s; (b) $t = 1920$ s; (c) $t = 6960$ s.

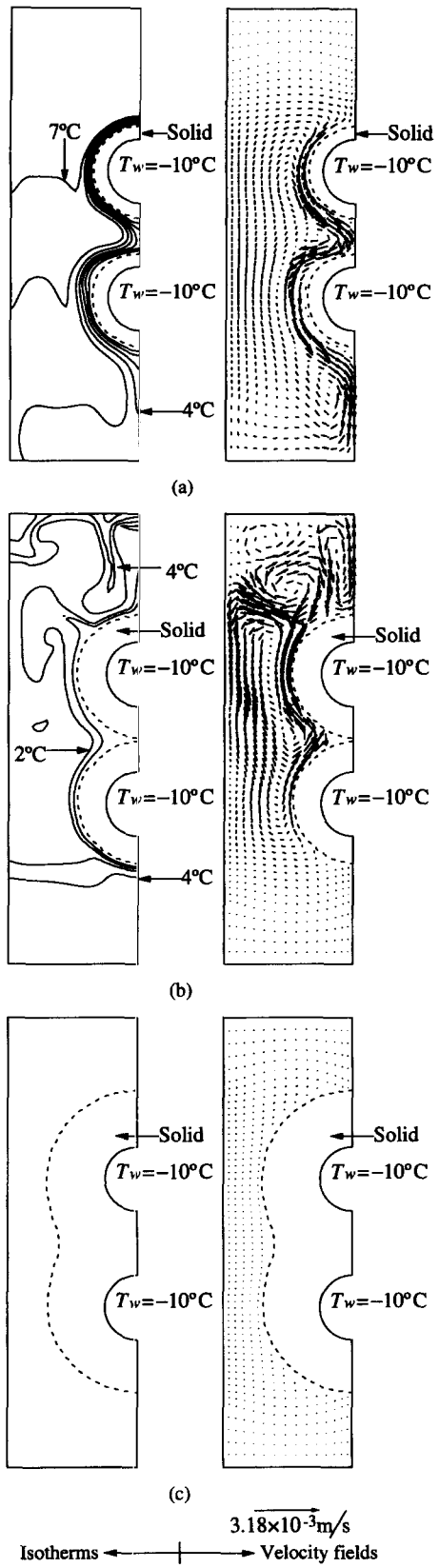

Fig. 12. Temperature (left panels) and velocity (right panels) fields and solid–liquid interface positions for the two-cylinder arrangement with $T_i = 8°C$ and $T_w = -10°C$: (a) $t = 480$ s; (b) $t = 1920$ s; (c) $t = 6960$ s.

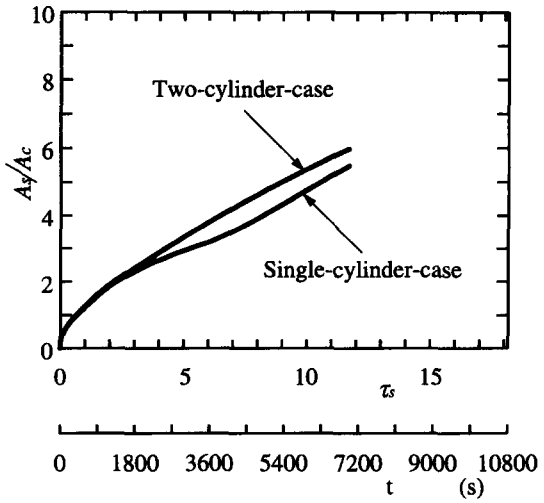

Fig. 13. Comparison of timewise variation of solid volume ratios for $T_i = 8°C$ and $T_w = -10°C$.

ally and the flow is weakened. Therefore, no strong and complicated flows are observed at $t = 6960$ s (Fig. 12(c)) and only a very weak counterclockwise circulation remains. The water temperature is reduced to nearly the fusion point in the entire cavity.

Figure 13 shows the timewise variations of the solid volume ratios for $T_i = 8°C$. It is seen that the ratio for the two-cylinder arrangement is larger than that for the single-cylinder. In general, the trend is similar to that for $T_i = 4°C$ (Fig. 10). However, a detailed comparison of the two figures reveals that for $T_i = 8°C$ the variation of A_s/A_c is different from that for $T_i = 4°C$. In the case of $T_i = 8°C$ for the single-cylinder, the cooling in the upper parts of the cavity is delayed for a while after the flow direction is changed, due to the small cold surface area, and, therefore, the solidification rate for the single-cylinder is decreased. But, the rate is increased after the water in the upper part of the cavity has been sufficiently cooled down. Therefore, in the case of $T_i = 8°C$, the difference between the solid volume ratios for the two-cylinder arrangement and for the single-cylinder becomes maximum at $t \approx 4000$ s, and from then on it decreases gradually, as is shown in Fig. 13.

3.5. *Results for* $T_i = 12°C$

Next, the results for the largest initial-temperature ($T_i = 12°C$) examined in this study are shown in Figs. 14–16. In Figs. 14 and 15, the difference between any two isotherms is 2°C. For the single-cylinder, downward flow arises at early times (Fig. 14(a)), and the dense water with a temperature of about 4°C accumulates under the cylinder, reducing the strength of the downflow. At $t = 3840$ s (Fig. 14(b)), a weak upward flow emerges, and the flow under the cylinder almost disappears due to the thermal stratification. In addition, hot water with temperature ranging between 8°C and 12°C forms a thermally stable layer above the cylinder. Thus, the upward flow is restricted to a

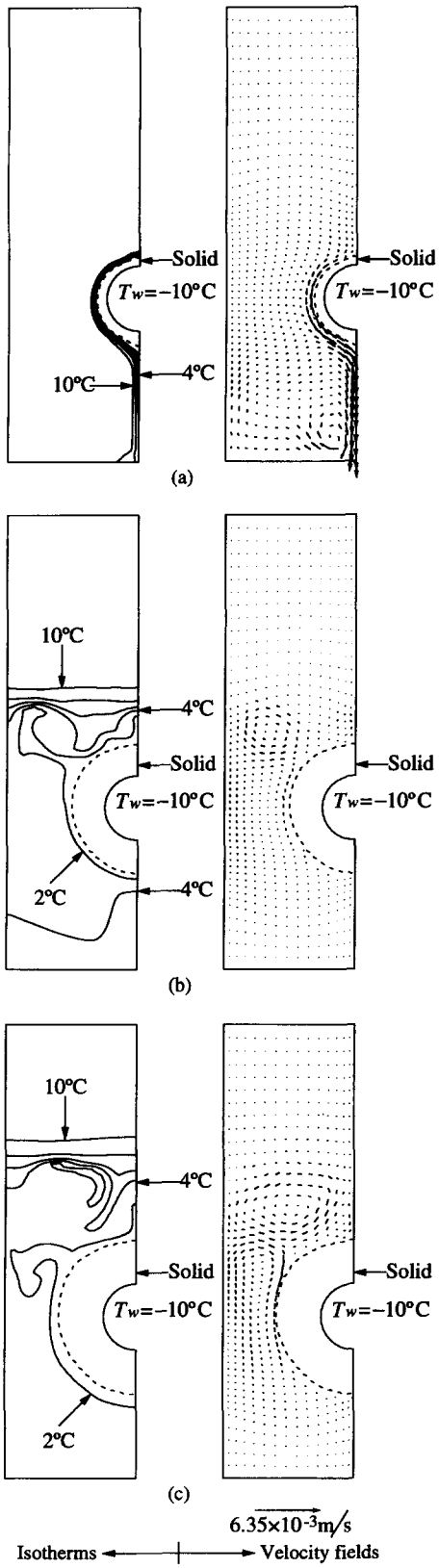

Fig. 14. Temperature (left panels) and velocity (right panels) fields and solid–liquid interface positions for the single-cylinder with $T_i = 12°C$ and $T_w = -10°C$: (a) $t = 480$ s; (b) $t = 3840$ s; (c) $t = 6960$ s.

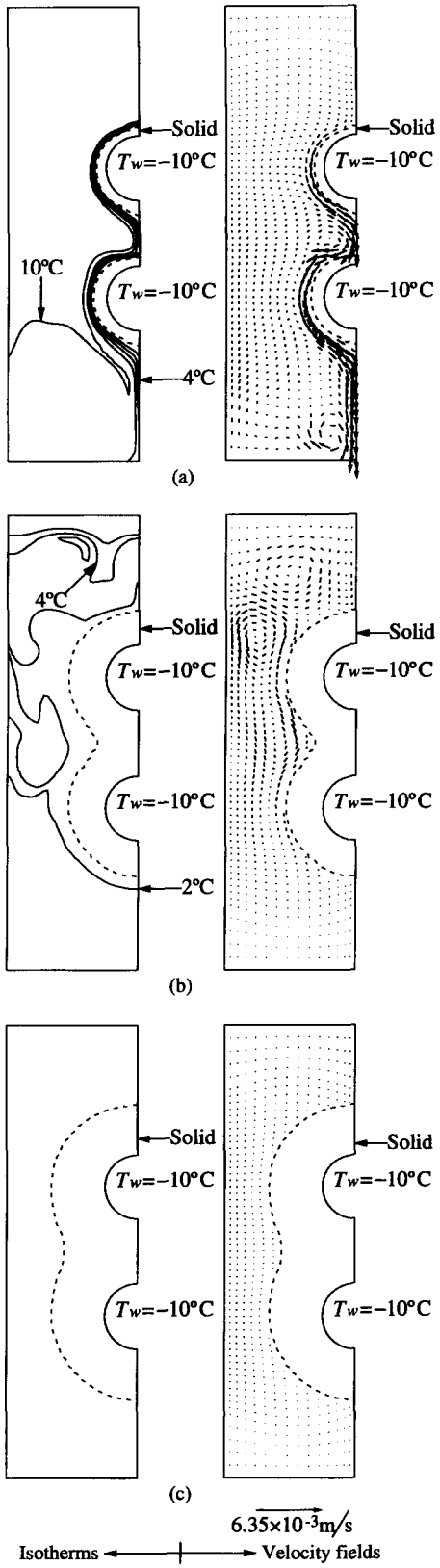

Fig. 15. Temperature (left panels) and velocity (right panels) fields and solid–liquid interface positions for the two-cylinder arrangement with $T_i = 12°C$ and $T_w = -10°C$: (a) $t = 480$ s; (b) $t = 3840$ s; (c) $t = 6960$ s.

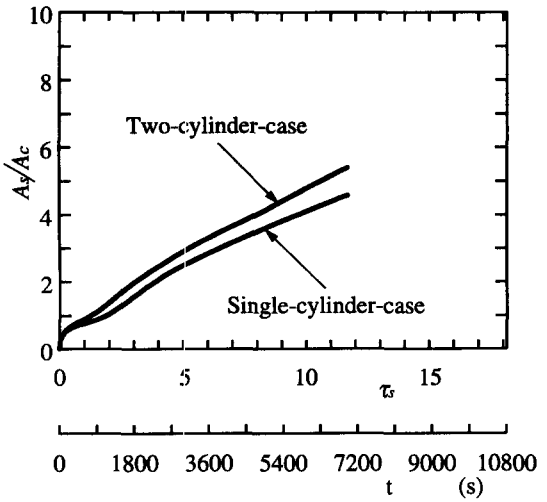

Fig. 16. Comparison of timewise variation of solid volume ratios for $T_i = 12°C$ and $T_w = -10°C$.

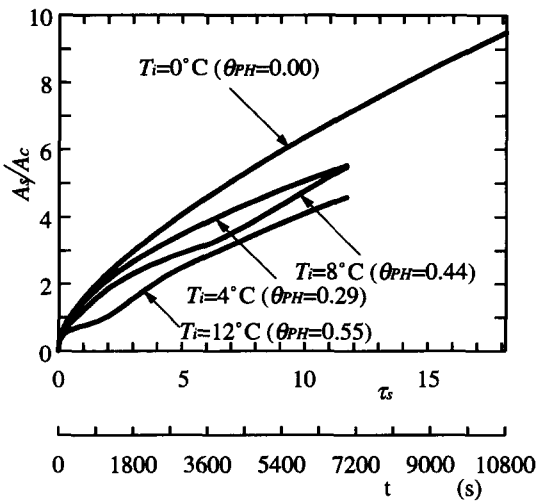

Fig. 17. The effect of the initial water temperature on timewise variation of solid volume ratios for the single-cylinder.

region where the temperature between 0°C and 4°C is contained by the upper and lower stratification layers. Even as time progresses to $t = 6969$ s (Fig. 14(c)), the stratification in the upper region still persists.Thus, the upward flow becomes only slightly stronger and effective mixing does not occur, compared with the case of $T_i = 8°C$ (Fig. 11).

For the two-cylinder arrangement (Fig. 15), a strong downward flow at early times changes to an upward flow (compare Fig. 15(a) with (b)) as for the single-cylinder. However, the upper cylinder for the two-cylinder arrangement effectively cools down the upper stratified layer. Therefore, the water temperature is uniformly reduced to approximately the fusion temperature, as is illustrated in Fig. 15(c).

From Fig. 16, it is seen that the solidification rates for the single-cylinder and the two-cylinder arrangement are increased at $t = 1200$ s and 1000 s, respectively. This is because the cooled water surrounding the solidified layer(s) prevents the hot stratified fluid layer in the upper part of the cavity from approaching the cylinder(s). The solidification rate for the single-cylinder becomes smaller than that for the two-cylinder arrangement at late times. This is due to the fact that the hot stratified layer above the cylinder remains for a longer period in the single-cylinder than that in the two-cylinder arrangements. It is also found that the solidification rate for $T_i = 12°C$ is smaller than those for $T_i = 4°C$ (Fig. 10) and 8°C (Fig. 13) at early stages of the freezing process because of the strong flow of warm water towards the interface. In addition, the difference between the solid volume ratios, A_s/A_c, for the single-cylinder and for the two-cylinder arrangements appears at an earlier stage as the initial water temperature, T_i is increased.

Finally, in order to clarify the effect of the initial water temperature, Figs. 6, 10, 13 and 16 are replotted together in Figs. 17 and 18 for the single-cylinder and for the two-cylinder arrangement, respectively. It is

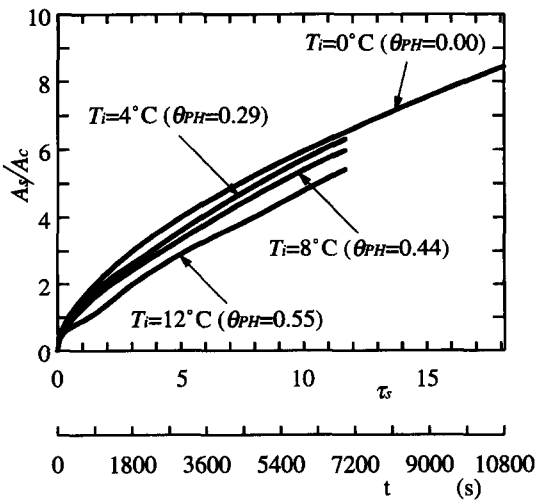

Fig. 18. The effect of the initial water temperature on timewise variation of solid volume ratios for the two-cylinder arrangement.

seen that the solid volume ratio is smaller for larger initial water temperature for both arrangements. The solidification rate varies in a more complicated manner for the single-cylinder (Fig. 17) with $T_i = 8°C$ and 12°C compared to the case of the two-cylinder arrangement (Fig. 18). This is because water with a temperature of about 4°C surrounds the cylinder for a longer time in the case of the single-cylinder, a shown in Figs. 11 and 14.

4. CONCLUSIONS

Extending a numerical model perviously proposed by the authors [11] and using the general coordinate system, a new numerical model is proposed to analyze solid–liquid phase change heat transfer in a complicated geometry. The present model can treat the solid/liquid phase change heat transfer with or with-

out porous media and it can also treat conventional (without phase change) transient natural convection with or without porous media filling the cavity. With the new model, numerical calculations were performed for solidification of pure water in the absence of porous media around a single and two cylinder arrangements to validate the model and to examine the effect of the interaction of two solidified layers on the freezing process. Based on the results obtained, the conclusions are summarized as follows:

(1) The numerically predicted interface shapes around the single and two cylinder(s) for the initial water temperature, T_i of 4°C were in excellent agreement with experimental results, validating the present numerical model.

(2) For $T_i = 0$°C the solidification rate (increasing rate of the solid volume ratio, A_s/A_c, with respect to time) is smaller for the two-cylinder arrangement than that for the single-cylinder. On the other hand, for $T_i \geqslant 4$°C the solidification rate is greater for the two-cylinder arrangement than that for the single-cylinder.

(3) For $T_i = 8$°C and 12°C, the flow direction is changed as time progresses so that the solidification rate is greatly affected. In particular, for $T_i = 12$°C two thermally stratified fluid layers appear at the top and bottom parts of the cavity, and the flow patterns and the temperature distributions become very complicated.

(4) The solidification rate varies in a complicated manner for the single-cylinder with $T_i = 8$°C and 12°C compared to the case of the two-cylinder arrangement.

In this study, we performed calculations only for a enclosure with a specific height and width as well as a specific position of cylinders, as shown in Fig. 1. If we consider an enclosure with a different size or with a different arrangement of cylinders, the feature of natural convection may largely change and therefore the solidification process may be considerably affected. The proposed numerical model can also treat other interesting solid–liquid phase change heat transfer problems in complicated geometries including melting and solidification of PCM around many cylinders embedded in porous media. The authors will conduct numerical simulations to examine these subjects in the near future.

REFERENCES

1. Bathelt, A.G. and Viskanta, R., Heat transfer at the solid–liquid interface during melting from a horizontal cylinder. *International Journal of Heat and Mass Transfer*, 1980, **23,** 1493–1503.
2. Sasaguchi, K. and Viskanta, R., An experimental study of simultaneous melting and solidification around two horizontal, vertically spaced cylinders. *Experimental Heat Transfer*, 1987, **1,** 223–236.
3. Sasaguchi, K. and Viskanata, R., Phase change heat transfer during melting and resolidification of melt around cylindrical heat source(s)/sink(s). *ASME Journal of Energy Resources Technology*, 1989, **111,** 43–49.
4. Bathelt, A. G., Viskanata, R. and Leidenfrost, W., Latent heat-of-fusion energy storage: experiments on heat transfer from cylinders during melting. *ASME Journal of Heat Transfer*, 1979, **101,** 453–458.
5. Cheng, K. C., Inaba, H. and Gilpin, R. G., Effect of natural convection on ice formation around an isothermally cooled horizontal cylinder. *ASME Journal of Heat Transfer*, 1988, **110,** 931–937.
6. Inaba, H., Freezing phenomena of a horizontal cooling cylinder in water at rest. *Refrigeration* (in Japanese) 1983, **58,** 651.
7. Narumi, A. and Kashiwagi, T., Freezing of supercooled water around two horizontal, vertically spaced cylinders. *Proceedings of Twenty-Seventh National Heat Transfer Symposium of Japan* (in Japanese), 1990, pp. 235–237.
8. Torikoshi, K., Nakasawa, Y. and Yamashita, H., An experimental study of melting of ice about horizontal cylinders. *Proceedings of Twenty-Sixth National Heat Transfer Symposium of Japan* (in Japanese), 1989, pp. 580–582.
9. Sasaguchi, K., Kusano, K. and Kitagawa, H., Solid–liquid phase change heat transfer around two horizontal, vertically spaced cylinders (an experimental study on the effect of density inversion of water). *Transactions of the JSME*, 1995, **61B,** 208–214.
10. Lacroix, M., Numerical simulation of melting and resolidification of a phase change material around two cylindrical heat exchangers. *Numerical Heat Transfer*, 1993, **24A,** 143–160.
11. Sasaguchi, K. and Takeo, H., Effect of orientation of a finned surface on the melting of frozen porous media. *International Journal of Heat and Mass Transfer*, 1994, **37,** 13–26.
12. Bennon, W. D. and Incropera, F. P., A continuum model for momentum, heat and species transport in binary solid–liquid phase change heat systems—I. Model formulation. *International Journal of Heat and Mass Transfer*, 1987, **30,** 2161–2170.
13. Sasaguchi, K., A single-domain model for analyzing heat transfer and fluid flow with solid/liquid phase change. *Science of Machines* (in Japanese), 1994, **46,** 931–936.
14. Gebhart, B. and Mollendorf, J., Buoyancy-induced flows in water under conditions in which density extrema may arise. *Journal of Fluid Mechanics*, 1978, **89,** 673–707.
15. Prakash, C. and Voller, V. R., On the numerical solution of continuum mixture model equations describing binary solid/liquid phase change. *Numerical Heat Transfer*, 1989, **15B,** 171–189.
16. Kusano, K., Solid–liquid phase change heat transfer around two horizontal cylinder(s) in a closed region. Ph.D. thesis (in Japanese), Kumamoto University, Japan, 1996.
17. Seger, J. L. and Soreson, R. L., Automatic mesh-point clustering near a boundary in grid generation with elliptic partial differential equations. *Journal of Computational Physics*, 1979, **33,** 405–410.
18. Takemoto, Y. and Nakamura, Y., Three-dimensional incompressible flow solver. In *Lecture Notes in Physics*, Vol. 264. Springer, Berlin, 1986, pp. 594–599.
19. Voller, V. R., Fast implicit finite-difference method for the analysis of phase change problem. *Numerical Heat Transfer*, 1990, **17B,** 155–169.